Article

Monovalent Copper Cation Doping Enables High-Performance CsPbIBr$_2$-Based All-Inorganic Perovskite Solar Cells

Zhaonan Du [1,†], Huimin Xiang [1,†], Amin Xie [1], Ran Ran [1], Wei Zhou [1], Wei Wang [1,*] and Zongping Shao [2,*]

1   State Key Laboratory of Materials-Oriented Chemical Engineering, College of Chemical Engineering, Nanjing Tech University, Nanjing 210009, China
2   WA School of Mines: Minerals, Energy and Chemical Engineering, Curtin University, Perth, WA 6845, Australia
*   Correspondence: wangwei@njtech.edu.cn (W.W.); zongping.shao@curtin.edu.au (Z.S.)
†   These authors contributed equally to this work.

Abstract: Organic–inorganic perovskite solar cells (PSCs) have delivered the highest power conversion efficiency (PCE) of 25.7% currently, but they are unfortunately limited by several key issues, such as inferior humid and thermal stability, significantly retarding their widespread application. To tackle the instability issue, all-inorganic PSCs have attracted increasing interest due to superior structural, humid and high-temperature stability to their organic–inorganic counterparts. Nevertheless, all-inorganic PSCs with typical CsPbIBr$_2$ perovskite as light absorbers suffer from much inferior PCEs to those of organic–inorganic PSCs. Functional doping is regarded as a simple and useful strategy to improve the PCEs of CsPbIBr$_2$-based all-inorganic PSCs. Herein, we report a monovalent copper cation (Cu$^+$)-doping strategy to boost the performance of CsPbIBr$_2$-based PSCs by increasing the grain sizes and improving the CsPbIBr$_2$ film quality, reducing the defect density, inhibiting the carrier recombination and constructing proper energy level alignment. Consequently, the device with optimized Cu$^+$-doping concentration generates a much better PCE of 9.11% than the pristine cell (7.24%). Moreover, the Cu$^+$ doping also remarkably enhances the humid and thermal durability of CsPbIBr$_2$-based PSCs with suppressed hysteresis. The current study provides a simple and useful strategy to enhance the PCE and the durability of CsPbIBr$_2$-based PSCs, which can promote the practical application of perovskite photovoltaics.

Keywords: CsPbIBr$_2$; perovskite solar cells; all-inorganic perovskites; Cu$^+$ doping; stability

1. Introduction

The energy crisis and greenhouse gas emissions are the most crucial worldwide problems nowadays, which are mainly caused by the low efficiency and excessive consumption of nonrenewable fossil fuels [1,2]. Thus, the utilization of renewable energies and the development of relevant energy conversion technologies are highly urgent and essential [3–7]. Among various types of renewable energies/sources, solar energy has gained particular interest due to its inexhaustible and clean nature, which can be efficiently utilized by three main routes: photovoltaic cells, photocatalysis and solar-thermal power generation [1,8–10]. In particular, photovoltaic cells (solar cells) have received increasing attention and achieved significant progress in the past decades because of their direct and efficient transformation of sunlight energy into electricity [11–15]. Nowadays, the commercial photovoltaic markets are dominated by silicon-based solar cells, showing excellent stability and high PCE of 27.6% [16]. However, silicon-based solar cells are limited by high-cost and complex fabrication procedures, and toxic by-products in the silicon manufacturing, which are harmful to the environment [17,18]. Consequently, the development of new-type solar cells with simple, cost-effective and environmentally friendly fabrication processes is highly crucial [19,20].

Among various third-generation solar cells, perovskite solar cells (PSCs) with halide perovskites as light absorbers are regarded as more attractive than dye-sensitized and organic solar cells due to the cheap raw materials used, the simple and low-cost fabrication procedures, as well as their rapidly increasing power conversion efficiencies (PCEs) in the last 10 years [21,22]. The theoretical limit of the PCE has been known for PSCs and is approximately 30% [23]. Since the invention of PSCs by Miyasaka et al. in 2009, typical organic–inorganic PSCs have witnessed a rapid increase in their PCEs from only 3.8% to over 25% due to several unique advantages of organic–inorganic halide perovskites, such as proper and adjustable band gaps, large light absorption coefficient, long diffusion length and superior mobility of carriers [24–27]. The general formula of halide perovskites is ABX_3, where A is monovalent cations including $CH_3NH_3^+$ (MA^+), $CH_3(NH_2)_2^+$ (FA^+) and cesium (Cs^+), B is divalent cations including Pb^{2+}, Sn^{2+} and Ge^{2+}, while X represents the halogen anions including I^-, Br^- and Cl^- [28–30]. It is well accepted that in addition to the PCEs, the long-term durability under humid, high-temperature and sunlight irradiation conditions is another key prerequisite for the widespread application of PSCs [31,32]. The plasmonic effect plays a very effective role in improving the efficiency of perovskite cells. By optimizing the adaptation of the plasmon photovoltaic channel, the relative efficiency was enhanced 40% [33]. Nevertheless, organic–inorganic hybrid PSCs suffer from inferior stability due to the high sensitivity of organic–inorganic perovskites against humidity, heat and light illumination, and they can be decomposed into PbI_2 because of the inherent volatility and hygroscopicity of organic A-site cations (e.g., MA^+, FA^+) in the organic–inorganic perovskites [34–37].

All-inorganic halide perovskites are considered as attractive alternatives to their organic–inorganic counterparts to tackle the above-mentioned instability issue due to having superior intrinsic structural stability and much lower sensitivity against humidity and heat [38,39]. During the past seven years, $CsPbI_xBr_{3-x}$ ($0 \leq x \leq 3$) as an important class of all-inorganic halide perovskites, has received particular attention as an efficient light absorber for PSCs due to the tunable band gaps, high intrinsic stability and superior carrier transport capability, etc. [40,41]. For instance, the PCEs of $CsPbI_3$-based PSCs with a proper band gap of 1.73 eV have reached 21% nowadays. However, $CsPbI_3$ perovskites suffer from the detrimental phase transformation from black $CsPbI_3$ non-perovskite yellow phase with a much wider band gap (3.01 eV) at room temperature, exhibiting negative impacts on the PCEs and the stability of $CsPbI_3$-based PSCs [42,43]. In contrast, $CsPbBr_3$ perovskites have exhibited excellent phase structural stability and high heat/moisture tolerance, which suffered from the extremely large band gap (2.3 eV), remarkably limiting sunlight absorption range and then the cell performance [44,45]. On this basis, mixed halide all-inorganic $CsPbIBr_2$ perovskite has attracted extensive interest due to the well-balanced band gap value (2.05 eV) and phase structural stability [46,47].

For single-junction PSCs, the calculated Shockley–Queisser limit is approximately 33%. Various approaches such as greatly increasing grain size, significantly reducing defect amount and band gaps, significantly improving carrier transport and separation capability, as well as constructing tandem PSCs, may allow approaching or surpassing the Shockley–Queisser limits of PSCs [3,48–50]. Nowadays, the PCEs of $CsPbIBr_2$-based PSCs have exceeded 12%, which is much inferior to the organic–inorganic PSCs [51,52]. It has been reported that the limited PCEs of $CsPbIBr_2$-based cells are mainly caused by the inferior quality $CsPbIBr_2$ films fabricated by the conventional solution route, exhibiting numerous pinholes, grain boundaries and defects, which functioned as recombination sites for photoinduced carriers to suppress the cell performance [53,54]. Therefore, a variety of strategies have been devoted to achieving high-quality $CsPbIBr_2$ light-absorbing films, such as interfacial modification, functional/selective cation doping, post-treatment process and additive engineering, etc. [55–57]. Among these available strategies, cation doping/substitution is widely employed to tailor the optical/electronic properties and film quality of $CsPbIBr_2$, which plays significant roles in creating homogeneous nucleation sites to control the crystallization and growth of $CsPbIBr_2$ crystals, contributing to remarkably

enhanced perovskite film quality [58–60]. Nowadays, the cation doping in $CsPbIBr_2$ is mainly focused on the utilization of divalent metal cations to substitute Pb^{2+}, including Sn^{2+}, Cu^{2+}, Zn^{2+}, Ba^{2+}, Eu^{2+}, etc., which effectively enhance the crystallinity and morphology of $CsPbIBr_2$ films [61–66]. For instance, Sn^{2+} plays a crucial role in regulating the band gap and enhancing the film quality of $CsPbIBr_2$, and Zhao et al. have reported that remarkably enhanced PCE (11.33%) and long-term stability were achieved by Sn^{2+} doping in $CsPbIBr_2$-based PSCs [61,64]. In our previous work, we have found that Cu^{2+} doping in $CsPbIBr_2$ with optimized doping concentration effectively inhibited the carrier recombination by reducing the defect amount, and it enhanced the perovskite film quality by improving the crystallinity and enlarging the grain sizes, thereby remarkably improving the PCEs and humid/thermal stability of $CsPbIBr_2$-based PSCs [62].

Nevertheless, it should be noted that the monovalent cation doping in the B-site of $CsPbIBr_2$ is much less investigated, which needs further exploration. Herein, we have employed monovalent copper cations (Cu^+) as effective B-site dopants for $CsPbIBr_2$ perovskites, which effectively improved the $CsPbIBr_2$ film quality in terms of a suppressed amount of grain boundaries, increased crystallinity and grain sizes, passivated surface defects and inhibited interfacial carrier recombination. After optimizing the Cu^+ doping concentration, the $CsPbIBr_2$-0.50%Cu cell produced a superb PCE of 9.11%, 25.8% higher than that of the pristine cell. Furthermore, Cu^+ doping also remarkably improved the high-temperature and humid durability of $CsPbIBr_2$-based PSCs with reduced hysteresis effect. Our current work can present some important insights for the design of high-performance all-inorganic PSCs, which may promote the widespread application of perovskite photovoltaics.

2. Materials and Methods

F^--doped tin oxide (FTO) glasses (2.2-mm thick and 7 Ω sq^{-1}) were first cleaned by various solvents, dried by N_2 and further treated by oxygen plasma cleaning [56]. Detailed information about the fabrication of $CsPbIBr_2$-based PSCs with a configuration of compact TiO_2 (c-TiO_2)/perovskite/2,2',7,7'-tetrakis (N,N-di-p-methoxyphenylamine)-9,9'-spirobifluorene (Spiro-OMeTAD)/Ag can be found in our previous work [62]. As for the Cu^+-doped $CsPbIBr_2$-based cells, different amounts of as-prepared 0.2 M cuprous bromide/dimethyl sulfoxide (CuBr/DMSO) solution were added into the 1 M $CsPbIBr_2$ precursor solution to prepare various Cu^+-doped $CsPbIBr_2$ films at fixed molar ratios of 0.25, 0.50 and 0.75%. The effective area of the cell was 0.0625 cm^2 in this work. For the thermal stability test, the carbon electrode was deposited by doctor blade for the hole-transporting layer (HTL)-free $CsPbIBr_2$-based PSCs and the detailed information can be found in our previous work [62].

X-ray diffraction (XRD) patterns of various samples were acquired by X-ray diffractometer (Rigaku Smartlab, Matsubara-cho, Tokyo, Japan) with Cu$K\alpha$ radiation. X-ray/ultraviolet photoelectron spectroscopy (XPS/UPS) profiles of various samples were acquired by XPS spectrometer (PHI5600 Versa Probe, Brooklyn, NY, USA). Energy-dispersive X-ray spectroscopy (EDX, Octane Ultra, Lafayette, LA, USA) and scanning electron microscope (SEM, Hitachi S-4800, Chiyoda-ku, Tokyo, Japan) were employed to investigate the microstructures and elemental mapping of various films. The surface roughness values of various perovskite films were acquired by atomic force microscopy (AFM, SmartSPM, Horiba, Minami-ku, Tokyo, Japan). Ultraviolet–visible (UV-vis) and photoluminescence (PL) spectra were obtained by Lambda 750 s spectrometer (PerkinElmer, Waltham, MA, USA) and fluorescence spectrometer (PerkinElmer, FL 6500, Waltham, MA, USA), respectively. Photocurrent density-voltage ($J-V$) curves of various cells were acquired by Zolix solar simulator under 1 Sun irradiation (100 mW cm^{-2}) after calibration. Electrochemical impedance spectroscopy (EIS) and external quantum efficiency (EQE) and spectra of various cells were acquired by electrochemical workstation (CHI760E) and Zolix Solar Cell Scan 100 instrument, respectively.

3. Results and Discussion

Cu^+ cations with three different molar ratios of 0.25, 0.50 and 0.75% were doped into $CsPbIBr_2$, which were labeled as $CsPbIBr_2$, $CsPbIBr_2$-0.25%Cu, $CsPbIBr_2$-0.50%Cu and $CsPbIBr_2$-0.75%Cu, respectively. Figure S1 displays the typical cross-sectional SEM image of as-fabricated $CsPbIBr_2$-0.50%Cu cell and it was found that the 350 nm-thick perovskite film was firmly adhered on the surface of c-TiO_2 film. Based on the $J-V$ curves of various $CsPbIBr_2$ cells, as depicted in Figure 1a and relevant photovoltaic parameters in Figure S2, the Cu^+ doping in $CsPbIBr_2$ significantly boosted the PCEs of corresponding cells by increasing the fill factor (FF) and short-circuit current density (J_{sc}). More specifically, the unmodified cell displayed a champion PCE of 7.24% with an open-circuit voltage (V_{oc}) of 1.16 V, a J_{sc} of 10.4 mA cm^{-2} and an FF of 0.597. In addition, the cell performance of Cu^+-doped $CsPbIBr_2$-based PSCs exhibited a volcano-like trend with increased Cu^+ doping contents, suggesting that the introduction of a suitable concentration of Cu^+ cations significantly enhanced the PCEs of $CsPbIBr_2$ cells. Particularly, the $CsPbIBr_2$-0.50%Cu cell displayed the highest PCE of 9.11%, with a V_{oc} of 1.19 V, a J_{sc} of 11.6 mA cm^{-2} and a FF of 0.658 (Table S1). The $CsPbIBr_2$-0.75%Cu cell exhibited a reduced PCE, which was mainly attributed to decreased FF value induced by the poor quality of $CsPbIBr_2$ film and higher defect concentration, which will be discussed later. Based on the EQE spectra in Figure 1b, the $CsPbIBr_2$-0.50%Cu cell displayed higher EQE values than those of the pristine cell at a wavelength range of 300 to 600 nm. In addition, $CsPbIBr_2$-0.50%Cu cell generated a larger integrated J_{sc} value of 9.7 mA cm^{-2} than that of the pristine cell (8.1 mA cm^{-2}), which was consistent with the $J-V$ results (Figure 1a). To confirm the universality of such PCE enhancement, 20 devices for each type of PSC (without and with 0.50%Cu^+ substitution) were fabricated and tested with the photovoltaic parameter distributions displayed in Figure 1c. It is clear that the average PCE of the $CsPbIBr_2$-0.50%Cu cell was much larger than that of the unmodified device due to the significantly improved J_{sc} and FF values (Figure S2). In addition, based on the maximum power point tracking (MPPT) profiles of PSCs as depicted in Figure 1d, the $CsPbIBr_2$-0.50%Cu cell produced much larger stabilized PCE and J_{sc} values than those of the pristine $CsPbIBr_2$ cell at the maximum power point.

It is well accepted that the PCEs of PSCs are determined by several crucial factors including the transport and recombination behavior of photogenerated carriers, defect density, sunlight absorption capability and energy level alignment between various films [67,68]. In order to elucidate the impacts of Cu^+ substitution on the $CsPbIBr_2$ film quality and the performance of $CsPbIBr_2$-based PSCs, we employed XRD technique to investigate the crystallinity and the crystal structures of pristine $CsPbIBr_2$ and various Cu^+-doped $CsPbIBr_2$ films. As depicted in Figure 2a, main characteristic peaks assigned to the α-phase $CsPbIBr_2$ structure were observed in all samples, while no obvious impurity phases were found for all investigated films, revealing that Cu^+ doping at different concentrations exhibited no obvious influences on the pure-phase cubic structure of $CsPbIBr_2$. Based on the magnified XRD peaks in Figure 2b, the characteristic XRD peaks gradually shifted to higher angles with the increased Cu^+ doping amounts, implying that the Cu^+ cations with smaller ionic radius (0.60 Å) than that of Pb^{2+} (1.19 Å) were successfully doped in the lattice of $CsPbIBr_2$ with a lattice contraction [69,70]. UV-vis absorption spectra were employed to evaluate the impacts of Cu^+ substitution on the light absorption capability of $CsPbIBr_2$ film. As depicted in Figure 2c, the Cu^+ doping effectively increased the light absorption intensity of $CsPbIBr_2$ film at 450–600 nm, especially for the $CsPbIBr_2$-0.50%Cu film. Based on the Tauc plots of various films acquired from the UV-vis spectra in Figure S3, the band gap values of $CsPbIBr_2$, $CsPbIBr_2$-0.25%Cu, $CsPbIBr_2$-0.50%Cu and $CsPbIBr_2$-0.75%Cu were calculated to be 2.08, 2.07, 2.07 and 2.06 eV, respectively. It can be concluded that the Cu^+ doping can improve the light absorption capability of $CsPbIBr_2$ film, although the Cu^+ doping displayed no obvious influences on the band gap values of $CsPbIBr_2$, which may be beneficial for the PCE improvement of corresponding PSCs. Based on the steady-state PL spectra of various $CsPbIBr_2$ films as depicted in Figure 2d, the Cu^+-doped $CsPbIBr_2$ films exhibited much lower PL intensity than the $CsPbIBr_2$ film, demonstrating that the carrier

recombination was effectively suppressed after introducing Cu^+ cations to reduce the defect amount. Moreover, $CsPbIBr_2$-0.75%Cu film with excessive Cu^+ doping amount displayed a higher PL intensity than that of $CsPbIBr_2$-0.50%Cu, implying more defects were formed in the $CsPbIBr_2$-0.75%Cu film, agreeing well with the $J-V$ results. It should be noted that the PL spectra of Cu^+-doped $CsPbIBr_2$ films exhibited several split peaks due to the phase segregation of $CsPbIBr_2$ films, which may be beneficial for the PCE enhancement [62,71]. Based on the TRPL spectra as depicted in Figure S4, $CsPbIBr_2$-0.50%Cu film delivered a much higher average carrier lifetime of 3.21 ns than the $CsPbIBr_2$ film (0.88 ns) due to the effectively suppressed defect concentration, which was favorable for the transport and separation of carriers. XPS was further employed to explore the influences of Cu^+ substitution on the chemical states of various ions in $CsPbIBr_2$ films, with results displayed in Figure S5. All the XPS peaks of $CsPbIBr_2$-0.50%Cu film shifted to lower binding energies compared with the $CsPbIBr_2$ film due to the shrinkage of the BX_6 octahedron caused by Cu^+ doping induced by the changed interatomic force [58,72].
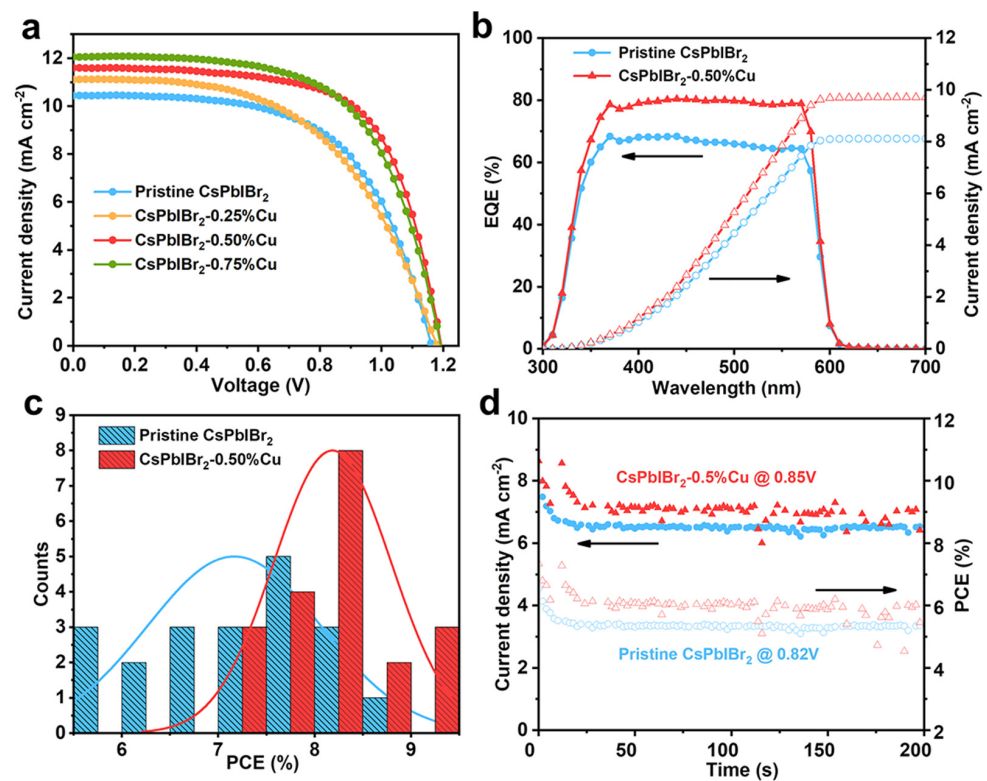
Figure 1. (**a**) $J-V$ curves of $CsPbIBr_2$ and various Cu^+-doped $CsPbIBr_2$ cells under a reverse scan direction. (**b**) EQE profiles, integrated photocurrent densities based on $CsPbIBr_2$ and $CsPbIBr_2$-0.50%Cu devices, (**c**) statistical PCE distributions of PSCs based on $CsPbIBr_2$ and $CsPbIBr_2$-0.50%Cu, (**d**) steady PCE and J_{sc} values of $CsPbIBr_2$ and $CsPbIBr_2$-0.50%Cu cells.
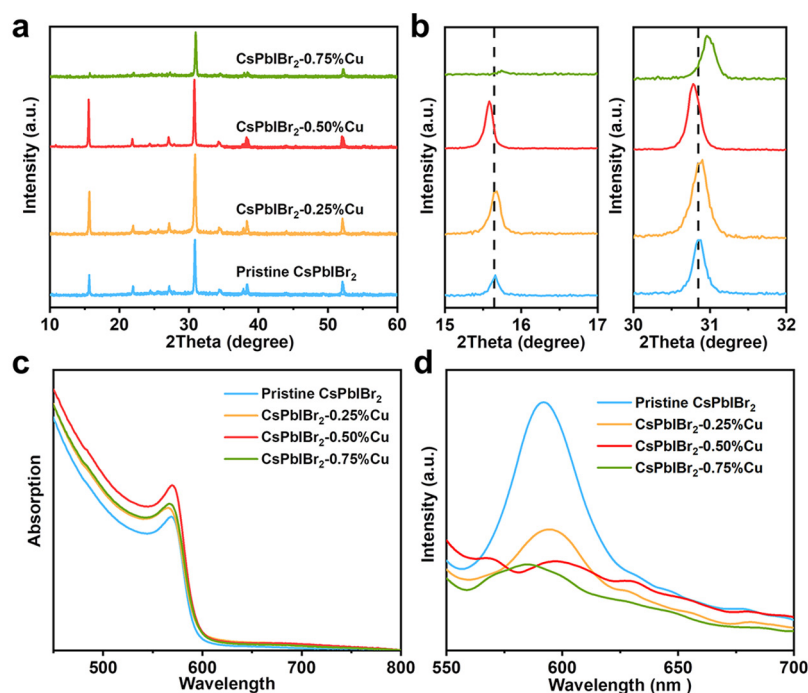
Figure 2. (**a**) XRD patterns, (**b**) magnified (100) and (200) peaks, (**c**) UV-vis and (**d**) PL spectra (deposited on conductive substrate) of $CsPbIBr_2$ and different Cu^+-doped $CsPbIBr_2$ films.

The morphology and quality of perovskite film plays a vital role in governing the performance of PSCs [54,73]. More specifically, compact perovskite films with large grain sizes and few grain boundaries are beneficial to suppress the carrier recombination [13,74]. Based on the top-view SEM images of $CsPbIBr_2$ and various Cu^+-doped $CsPbIBr_2$ films in Figure 3a–d and Figure S6, the pristine $CsPbIBr_2$ film displayed an inferior morphology with abundant pinholes and small grains, while the quality of $CsPbIBr_2$ film was significantly improved after Cu^+ doping in terms of reduced amount of pinholes and larger grain sizes. Particularly, the $CsPbIBr_2$-0.50%Cu film showed a dense and uniform morphology with remarkably enlarged grain sizes and reduced amount of grain boundaries (Figure 3c,d). Nevertheless, $CsPbIBr_2$-0.75%Cu film with excessive Cu^+ doping amount exhibited smaller grain sizes than those of $CsPbIBr_2$-0.50%Cu film, as displayed in Figure S6c,d. In addition, it was found that all elements were uniformly distributed on the $CsPbIBr_2$-0.50%Cu film, as depicted in Figure 3e, demonstrating homogeneous distribution of Cu^+ dopants. Based on the AFM images as depicted in Figure 3f,g and Figure S7, the $CsPbIBr_2$-0.50%Cu film delivered a lower root-mean-square (RMS) surface roughness of 29.9 nm than the $CsPbIBr_2$ film (31.3 nm), benefiting the interfacial charge transfer at perovskite film/HTL interface [75,76].

The carrier recombination behavior of $CsPbIBr_2$ film after Cu^+ doping was investigated by EIS at a fixed voltage of 0.5 V under dark conditions, as depicted in Figure 4a. As can be seen, a low-frequency arc corresponding to the recombination resistance (R_{rec}) existed in the Nyquist plots, which was inversely proportional to the degree of carrier recombination at the interfaces between the perovskite films and TiO_2/Spiro-OMeTAD layer [77,78]. The $CsPbIBr_2$-0.50%Cu cell generated a larger R_{rec} value than the $CsPbIBr_2$ cell, suggesting that the Cu^+ doping remarkably suppressed the interfacial carrier recombination. Based on the dark $J−V$ curves as displayed in Figure 4b, the $CsPbIBr_2$-0.50%Cu cell delivered much smaller current densities than those of the pristine $CsPbIBr_2$ cell, demonstrating that the photo-generated carriers were efficiently transported through charge-transporting layers of the $CsPbIBr_2$-0.50%Cu cell instead of direct shunting, leading to reduced voltage/current loss and enhanced cell performance, which was attributed to the improved morphology and quality of $CsPbIBr_2$-0.50%Cu films.
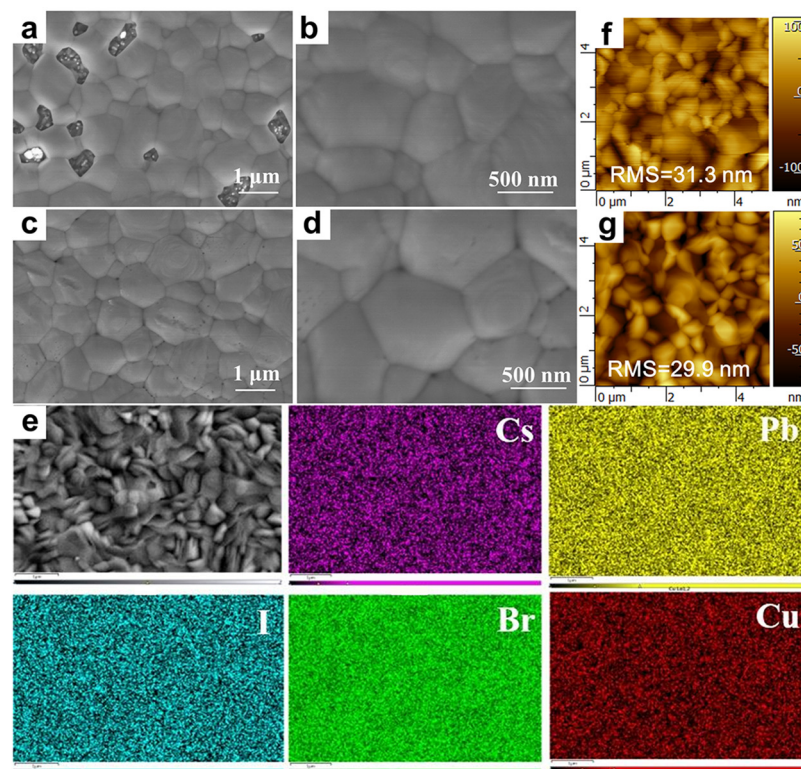
Figure 3. Top-view SEM images of (**a**,**b**) CsPbIBr$_2$ and (**c**,**d**) CsPbIBr$_2$-0.50%Cu films at different magnifications. (**e**) EDX elemental mapping images of CsPbIBr$_2$-0.50%Cu film including Cs, Pb, I, Br, Cu elements. Top-view AFM images of (**f**) CsPbIBr$_2$ and (**g**) CsPbIBr$_2$-0.50%Cu films.
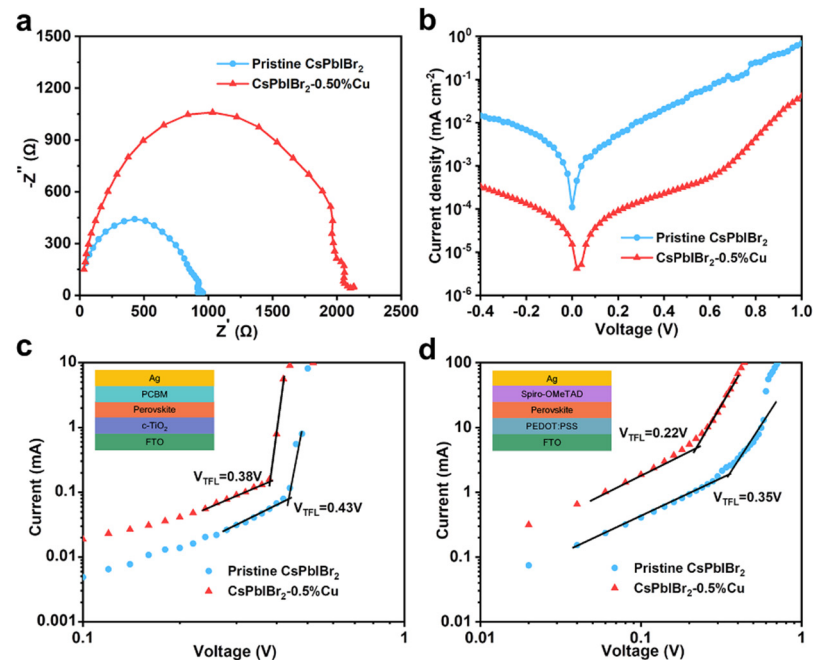
Figure 4. (**a**) EIS spectra and (**b**) $J-V$ curves of CsPbIBr$_2$ and CsPbIBr$_2$-0.50%Cu cells in the dark. Dark $J-V$ curves of (**c**) electron-only and (**d**) hole-only PSCs based on CsPbIBr$_2$ and CsPbIBr$_2$-0.50%Cu.

Hole-only and electron-only PSCs with structures of FTO/PEDOT:PSS/pervoskite/ Spiro-OMeTAD/Ag and FTO/TiO$_2$/pervoskite/[6,6]-phenyl-C61-butyric acid methyl ester (PCBM)/Ag were prepared to determine the trap densities of PSCs by measuring the dark $J-V$ curves using the space charge-limiting current model [13,79]. As shown in Figure 4c,d,

the traps were gradually filled until the applied voltage reached the trap-filling-limit voltage (V_{TFL}). The trap densities (N_{defects}) can be estimated by the equation of $N_{\text{defects}} = \frac{2\varepsilon\varepsilon_0 V_{\text{TFL}}}{eL^2}$, where ε is the relative dielectric constant of $CsPbIBr_2$ (approximately 8); ε_0 is the vacuum dielectric constant; e represents elementary charge; and L is the thickness of $CsPbIBr_2$ film (350 nm, Figure S1). The V_{TFL} values were 0.43 and 0.38 V for electron-only devices with $CsPbIBr_2$ and $CsPbIBr_2$-0.50%Cu films, corresponding to trap densities of 3.10 and 2.75×10^{15} cm^{-3}, respectively. As for hole-only devices, the hole defect densities of $CsPbIBr_2$ and $CsPbIBr_2$-0.50%Cu films were 3.90 and 1.59×10^{15} cm^{-3} based on V_{TFL} values of 0.54 and 0.22 V, respectively. This suggested that the Cu$^+$ doping effectively reduced the trapping centers for both electrons and holes of $CsPbIBr_2$ film.

UPS technique was used to explore the effects of Cu$^+$ substitution on the energy level alignment of $CsPbIBr_2$-based PSCs. As displayed in Figure S8 and Table S2, the valence band maximum (E_{VBM}) was calculated as -5.58 and -5.52 eV for $CsPbIBr_2$ and $CsPbIBr_2$-0.50%Cu, respectively, while the corresponding conduction band minimum (E_{CBM}) was calculated to be -3.50 and -3.45 eV, respectively, based on the relationship of band gap = $E_{\text{CBM}} - E_{\text{VBM}}$ [80]. In addition, the Fermi level of $CsPbIBr_2$ was slightly increased from -3.74 to -3.68 eV after the introduction of 0.50% Cu$^+$, which was closer to the CBM position (-3.51 eV) due to the n-type nature of Cu$^+$-doped $CsPbIBr_2$ [81]. The upshifted VBM position of $CsPbIBr_2$-0.50%Cu effectively promoted the hole extraction from Spiro-OMeTAD to the perovskite layer. Moreover, the larger energy differences between the CBMs of $CsPbIBr_2$-0.50%Cu and TiO_2 may provide a higher driving force for the electron injection from light-absorbing film to the electron-transporting layer [72]. Furthermore, the hysteresis index of the $CsPbIBr_2$ cell was reduced from 0.48 to 0.43 after the introduction of 0.50%Cu based on the $J-V$ curves of corresponding PSCs under reverse and forward scan directions (Figure S9 and Table S3), which was attributed to the improved $CsPbIBr_2$ film quality and promoted charge transfer, benefiting the cell stability.

Besides the device efficiency, the humid and thermal stability is another crucial factor for the development of PSCs. As depicted in Figure 5a, the $CsPbIBr_2$-0.50%Cu cell retained 94% of its primary PCE after storing in humid air with a relative humidity (RH) of 15–30% at 25 °C for 400 h, much superior to the pristine device (57%) under the same conditions. Furthermore, the PCE of the $CsPbIBr_2$-0.50%Cu cell maintained 80% after 600 h storage in ambient condition with a RH of 15–30%. The high-temperature air stability of PSCs was evaluated by preparing HTL-free cells (FTO/c-TiO$_2$/perovskite/carbon). The photovoltaic parameters of HTL-free $CsPbIBr_2$ and $CsPbIBr_2$-0.50%Cu cells are listed in Table S4. It was found that the $CsPbIBr_2$-0.50%Cu cell delivered a superior PCE retention ratio of 97% to that of the $CsPbIBr_2$ device (76%) after storing in ambient condition at 85 °C for 1000 h (Figure 5b).

Cu$^+$ involved in the lattice of $CsPbIBr_2$ partially substituted the Pb^{2+}-occupied B-site, causing a lattice contraction, and resulted in a reduced bandgap for Cu$^+$-doped $CsPbIBr_2$ film. The reduced bandgap is beneficial for broadening light absorption band edge, thus facilitating the increase of photocurrent density. A previous study suggested that lattice contraction caused by doping could lead to improved heat stability for PSCs [82]. The presence of grain boundaries and pinholes might act as defect centers, trapping charge carriers, thereby reducing the PCE of PSC [83] Homogeneous and compact perovskite morphology with large grain sizes, less grain boundaries and pinholes enhanced the light capture of Cu$^+$-doped perovskite film. The chemical bonds were enhanced after Cu$^+$ doping, leading to higher phase stability [84]. Moreover, the defect density and the nonradiative recombination of the films were reduced.
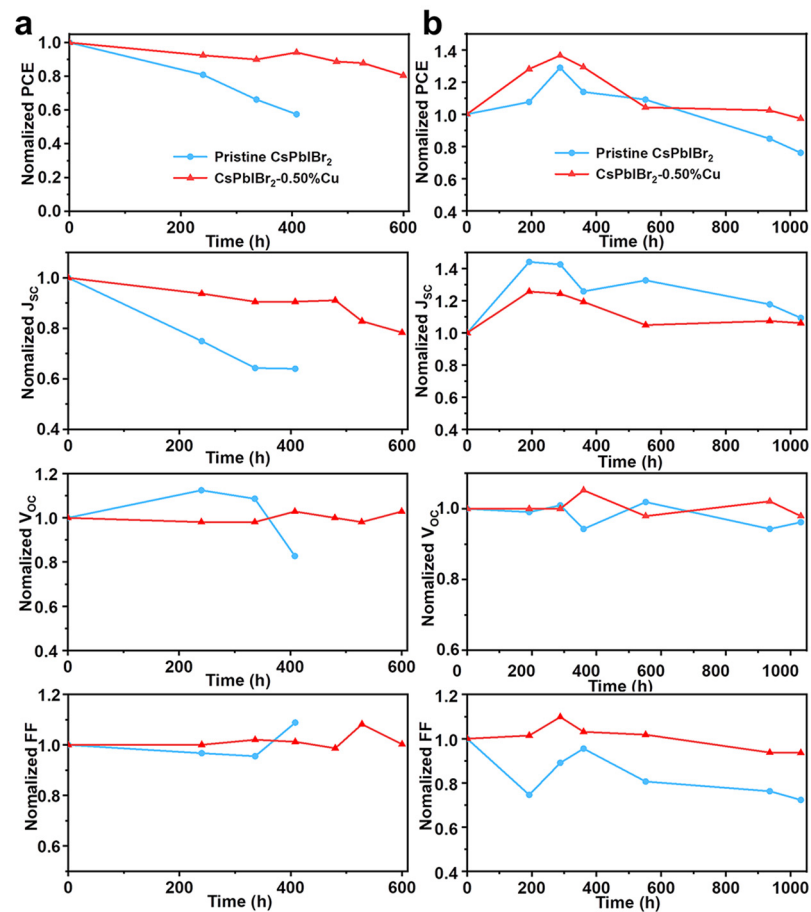
Figure 5. Normalized photovoltaic parameters of CsPbIBr$_2$ and CsPbIBr$_2$-0.50%Cu cells stored in humid air at (**a**) 25 °C and (**b**) 85 °C without encapsulation.

4. Conclusions

In summary, we report a monovalent Cu$^+$ cation doping approach to boost the PCEs and humid/thermal durability of CsPbIBr$_2$-based all-inorganic PSCs. It was found that the introduction of a proper amount of Cu$^+$ cations into CsPbIBr$_2$ effectively passivated the defects, improved the perovskite film quality, suppressed the interfacial carrier recombination and enhanced the energy level alignment. Consequently, the optimized Cu$^+$-doped cell exhibited a superb PCE of 9.11% with reduced hysteresis, which was 25.8% higher than that of pristine cell (7.24%). Moreover, the Cu$^+$ doping also remarkably improved the thermal and humid stability of CsPbIBr$_2$-based PSCs. For instance, the CsPbIBr$_2$-0.50%Cu device retained 97% of the primary PCE after 1000 h storage at 85 °C in humid air, while the PCE of the pristine PSC declined to 76% under the same conditions. This work provides some important insights for the fabrication of durable CsPbIBr$_2$-based all-inorganic PSCs with higher PCEs, which may promote the commercialization of this technology.

Supplementary Materials: The following supporting information can be downloaded at: https://www.mdpi.com/article/10.3390/nano12234317/s1, Figure S1: Cross-sectional SEM images of CsPbIBr$_2$-based cell; Figure S2: (a) PCE, (b) J_{sc}, (c) V_{oc} and (d) FF distributions of CsPbIBr$_2$-based PSCs without and with 0.50% Cu$^+$ doping with the corresponding average values shown inside; Figure S3: Tauc plots of CsPbIBr$_2$ films with different Cu$^+$ doping concentrations; Figure S4: TRPL spectra of CsPbIBr$_2$ and CsPbIBr$_2$-0.50%Cu films; Figure S5: XPS spectra of the pristine CsPbIBr$_2$ and CsPbIBr$_2$-0.50%Cu films: (a) Cs 3d, (b) Pb 4f, (c) I 3d, (d) Br 3d and (e) XPS survey spectra; Figure S6: Top-view SEM images of the (a, b) CsPbIBr$_2$-0.25%Cu and (c, d) CsPbIBr$_2$-0.75%Cu films; Figure S7: 3D-AFM models of (a) pristine CsPbIBr$_2$ and (b) CsPbIBr$_2$-0.50%Cu films; Figure S8: UPS spectra of pristine CsPbIBr$_2$ and CsPbIBr$_2$-0.50%Cu films: (a) the cut-off energies (Ecut-off) and (b) the positions

of Fermi edge; Figure S9: *J–V* curves of (a) pristine $CsPbIBr_2$ and (b) $CsPbIBr_2$-0.50%Cu cells under revere and forward scan directions; Table S1: Photovoltaic performance parameters of $CsPbIBr_2$-based PSCs with different Cu^+ doping concentrations; Table S2: Calculated energy levels of pristine $CsPbIBr_2$ and $CsPbIBr_2$-0.50%Cu films; Table S3: Photovoltaic parameters of pristine $CsPbIBr_2$ and $CsPbIBr_2$-0.50%Cu cells under revere and forward scan directions; Table S4: Photovoltaic parameters of carbon-based HTL-free PSCs based on $CsPbIBr_2$ and $CsPbIBr_2$-0.50%Cu perovskites.

Author Contributions: Investigation, Z.D. and H.X.; conceptualization, W.W.; formal analysis, Z.D. and H.X.; visualization, Z.D.; writing—original draft, Z.D.; validation, Z.D.; data curation, Z.D., H.X. and A.X.; supervision, W.W. and Z.S.; writing—review and editing, R.R., W.W. and Z.S.; project administration, W.Z.; funding acquisition, W.Z., W.W. and Z.S. All authors have read and agreed to the published version of the manuscript.

Institutional Review Board Statement: Not applicable.

Informed Consent Statement: Not applicable.

Data Availability Statement: The data that support the findings of this study are available from the corresponding author upon reasonable request.

Conflicts of Interest: The authors declare no conflict of interest.

References

1. Lai, C.S.; Jia, Y.; Lai, L.L.; Xu, Z.; McCulloch, M.D.; Wong, K.P. A comprehensive review on large-scale photovoltaic system with applications of electrical energy storage. *Renew. Sustain. Energy Rev.* **2017**, *78*, 439–451. [CrossRef]
2. Zou, H.; Du, H.; Ren, J.; Sovacool, B.K.; Zhang, Y.; Mao, G. Market dynamics, innovation, and transition in China's solar photovoltaic (pv) industry: A critical review. *Renew. Sustain. Energy Rev.* **2017**, *69*, 197–206. [CrossRef]
3. Jacak, J.E.; Jacak, W.A. Routes for metallization of perovskite solar cells. *Materials* **2022**, *15*, 2254. [CrossRef]
4. Mitrašinović, A.M. Photovoltaics advancements for transition from renewable to clean energy. *Energy* **2021**, *237*, 121510. [CrossRef]
5. Carneiro, A.L.; Martins, A.A.; Duarte, V.C.M.; Mata, T.M.; Andrade, L. Energy consumption and carbon footprint of perovskite solar cells. *Energy Rep.* **2022**, *8*, 475–481. [CrossRef]
6. Qiao, Y.; Li, S.; Liu, W.; Ran, M.; Lu, H.; Yang, Y. Recent advances of rare-earth ion doped luminescent nanomaterials in perovskite solar cells. *Nanomaterials* **2018**, *8*, 43. [CrossRef] [PubMed]
7. Yang, X.; Wang, W.; Ran, R.; Zhou, W.; Shao, Z. Recent advances in $Cs_2AgBiBr_6$-based halide double perovskites as lead-free and inorganic light absorbers for perovskite solar cells. *Energy Fuels* **2020**, *34*, 10513–10528. [CrossRef]
8. Wang, W.; Xu, M.; Xu, X.; Zhou, W.; Shao, Z. Perovskite oxide based electrodes for high-performance photoelectrochemical water splitting. *Angew. Chem. Int. Ed.* **2020**, *59*, 136–152. [CrossRef]
9. He, J.; Liu, P.; Ran, R.; Wang, W.; Zhou, W.; Shao, Z. Single-atom catalysts for high-efficiency photocatalytic and photoelectro-chemical water splitting: Distinctive roles, unique fabrication methods and specific design strategies. *J. Mater. Chem. A* **2022**, *10*, 6835–6871. [CrossRef]
10. Han, X.; Liu, P.; Ran, R.; Wang, W.; Zhou, W.; Shao, Z. Non-metal fluorine doping in Ruddlesden-Popper perovskite oxide enables high-efficiency photocatalytic water splitting for hydrogen production. *Mater. Today Energy* **2022**, *23*, 100896. [CrossRef]
11. Muradov, A.; Frolushkina, D.; Samusenkov, V.; Zhamanbayeva, G.; Kot, S. Methods of stability control of perovskite solar cells for high efficiency. *Energies* **2021**, *14*, 2918. [CrossRef]
12. Park, H.H. Inorganic materials by atomic layer deposition for perovskite solar cells. *Nanomaterials* **2021**, *11*, 88. [CrossRef] [PubMed]
13. Liu, P.; Xiang, H.; Wang, W.; Ran, R.; Zhou, W.; Shao, Z. A bilateral cyano molecule serving as an effective additive enables high-efficiency and stable perovskite solar cells. *J. Energy Chem.* **2021**, *62*, 243–251. [CrossRef]
14. Fang, Z.; Zeng, Q.; Zuo, C.; Zhang, L.; Xiao, H.; Cheng, M.; Hao, F.; Bao, Q.; Zhang, L.; Yuan, Y.; et al. Perovskite-based tandem solar cells. *Chin. Sci. Bull.* **2021**, *66*, 621–636. [CrossRef]
15. Xiao, H.; Liu, P.; Wang, W.; Ran, R.; Zhou, W.; Shao, Z. Enhancing the photocatalytic activity of Ruddlesden-Popper Sr_2TiO_4 for hydrogen evolution through synergistic silver doping and moderate reducing pretreatment. *Mater. Today Energy* **2022**, *23*, 100899. [CrossRef]
16. Chen, B.; Wang, P.; Li, R.; Ren, N.; Han, W.; Zhu, Z.; Wang, J.; Wang, S.; Shi, B.; Liu, J.; et al. A two-step solution-processed wide-bandgap perovskite for monolithic silicon-based tandem solar cells with >27% efficiency. *ACS Energy Lett.* **2022**, *7*, 2771–2780. [CrossRef]
17. Xiang, H.; Liu, P.; Wang, W.; Ran, R.; Zhou, W.; Shao, Z. Towards highly stable and efficient planar perovskite solar cells: Materials development, defect control and interfacial engineering. *Chem. Eng. J.* **2021**, *420*, 127599. [CrossRef]

18. Ansari, M.I.H.; Qurashi, A.; Nazeeruddin, M.K. Frontiers, opportunities, and challenges in perovskite solar cells: A critical review. *J. Photochem. Photobiol. C* **2018**, *35*, 1–24. [CrossRef]

19. Huang, D.; Xiang, H.; Ran, R.; Wang, W.; Zhou, W.; Shao, Z. Recent advances in nanostructured inorganic hole-transporting materials for perovskite solar cells. *Nanomaterials* **2022**, *12*, 2592. [CrossRef]

20. Liu, P.; Wang, W.; Liu, S.; Yang, H.; Shao, Z. Fundamental understanding of photocurrent hysteresis in perovskite solar cells. *Adv. Energy Mater.* **2019**, *9*, 1803017. [CrossRef]

21. Shahinuzzaman, M.; Afroz, S.; Mohafez, H.; Jamal, M.S.; Khandaker, M.U.; Sulieman, A.; Tamam, N.; Islam, M.A. Roles of inorganic oxide based htms towards highly efficient and long-term stable PSC: A review. *Nanomaterials* **2022**, *12*, 3003. [CrossRef] [PubMed]

22. Wang, P.; Li, R.; Chen, B.; Hou, F.; Zhang, J.; Zhao, Y.; Zhang, X. Gradient energy alignment engineering for planar perovskite solar cells with efficiency over 23%. *Adv. Mater.* **2020**, *32*, 1905766. [CrossRef] [PubMed]

23. Seki, K.; Furube, A.; Yoshida, Y. Theoretical limit of power conversion efficiency for organic and hybrid halide perovskite photovoltaics. *Jpn. J. Appl. Phys.* **2015**, *54*, 08KF04. [CrossRef]

24. Kojima, A.; Teshima, K.; Shirai, Y.; Miyasaka, T. Organometal halide perovskites as visible-light sensitizers for photovoltaic cells. *J. Am. Chem. Soc.* **2009**, *131*, 6050–6051. [CrossRef]

25. NREL. Best Research-Cell Efficiency Chart. Available online: https://www.nrel.gov/pv/cell-efficiency.html (accessed on 13 November 2022).

26. Xiang, H.; Liu, P.; Ran, R.; Wang, W.; Zhou, W.; Shao, Z. Two-dimensional Dion-Jacobson halide perovskites as new-generation light absorbers for perovskite solar cells. *Renew. Sust. Energy Rev.* **2022**, *166*, 112614. [CrossRef]

27. Yang, X.; Xie, A.; Xiang, H.; Wang, W.; Ran, R.; Zhou, W.; Shao, Z. First investigation of additive engineering for highly efficient $Cs_2AgBiBr_6$-based lead-free inorganic perovskite solar cells. *Appl. Phys. Rev.* **2021**, *8*, 041402. [CrossRef]

28. Liu, H.; Xiang, L.; Gao, P.; Wang, D.; Yang, J.; Chen, X.; Li, S.; Shi, Y.; Gao, F.; Zhang, Y. Improvement strategies for stability and efficiency of perovskite solar cells. *Nanomaterials* **2022**, *12*, 3295. [CrossRef]

29. Mangrulkar, M.; Stevenson, K.J. The progress of additive engineering for $CH_3NH_3PbI_3$ photo-active layer in the context of perovskite solar cells. *Crystals* **2021**, *11*, 814. [CrossRef]

30. Shen, W.; Dong, Y.; Huang, F.; Cheng, Y.; Zhong, J. Interface passivation engineering for hybrid perovskite solar cells. *Mater. Rep. Energy* **2021**, *1*, 100060. [CrossRef]

31. Sathiyan, G.; Syed, A.A.; Chen, C.; Wu, C.; Tao, L.; Ding, X.; Miao, Y.; Li, G.; Cheng, M.; Ding, L. Dual effective dopant based hole transport layer for stable and efficient perovskite solar cells. *Nano Energy* **2020**, *72*, 104673. [CrossRef]

32. Zhang, J.; Che, B.; Zhao, W.; Fang, Y.; Han, R.; Yang, Y.; Liu, J.; Yang, T.; Chen, T.; Yuan, N.; et al. Polar species for effective dielectric regulation to achieve high-performance $CsPbI_3$ solar cells. *Adv. Mater.* **2022**, *34*, 2202735. [CrossRef] [PubMed]

33. Laska, M.; Krzemińska, Z.; Kluczyk-Korch, K.; Schaadt, D.; Popko, E.; Jacak, W.A.; Jacak, J.E. Metallization of solar cells, exciton channel of plasmon photovoltaic effect in perovskite cells. *Nano Energy* **2020**, *75*, 104751. [CrossRef]

34. Lee, J.; Park, N. Chemical approaches for stabilizing perovskite solar cells. *Adv. Energy Mater.* **2020**, *10*, 1903249. [CrossRef]

35. Maafa, I.M. All-inorganic perovskite solar cells: Recent advancements and challenges. *Nanomaterials* **2022**, *12*, 1651. [CrossRef]

36. Eze, V.O.; Carani, L.B.; Majumder, H.; Uddin, M.J.; Okoli, O.I. Inorganic cesium lead mixed halide based perovskite solar materials modified with functional silver iodide. *Sci. Rep.* **2022**, *12*, 7794. [CrossRef] [PubMed]

37. Liu, L.; Lu, J.; Wang, H.; Cui, Z.; Giorgi, G.; Bai, Y.; Chen, Q. A-site phase segregation in mixed cation perovskite. *Mater. Rep. Energy* **2021**, *1*, 100064. [CrossRef]

38. Zhai, M.; Wang, A.; Chen, C.; Hao, F.; Wang, H.; Ding, L.; Yang, X.; Cheng, M. Construct efficient $CsPbI_2Br$ solar cells by minimizing the open-circuit voltage loss through controlling the peripheral substituents of hole-transport materials. *Chem. Eng. J.* **2021**, *425*, 131675. [CrossRef]

39. Wang, Y.; Chen, Y.; Zhang, T.; Wang, X.; Zhao, Y. Chemically stable black phase $CsPbI_3$ inorganic perovskites for high-efficiency photovoltaics. *Adv. Mater.* **2020**, *32*, 2001025. [CrossRef]

40. Protesescu, L.; Yakunin, S.; Bodnarchuk, M.I.; Krieg, F.; Caputo, R.; Hendon, C.H.; Yang, R.X.; Walsh, A.; Kovalenko, M.V. Nanocrystals of cesium lead halide perovskites ($CsPbX_3$, X = Cl, Br, and I): Novel optoelectronic materials showing bright emission with wide color gamut. *Nano Lett.* **2015**, *15*, 3692–3696. [CrossRef]

41. Xiang, W.; Liu, S.; Tress, W. Interfaces and interfacial layers in inorganic perovskite solar cells. *Angew. Chem. Int. Ed.* **2021**, *60*, 26440–26453. [CrossRef]

42. Cui, Y.; Shi, J.; Meng, F.; Yu, B.; Tan, S.; He, S.; Tan, C.; Li, Y.; Wu, H.; Luo, Y.; et al. A versatile molten-salt induction strategy to achieve efficient $CsPbI_3$ perovskite solar cells with a high open-circuit voltage >1.2 V. *Adv. Mater.* **2022**, *34*, 2205028. [CrossRef] [PubMed]

43. Marronnier, A.; Roma, G.; Boyer-Richard, S.; Pedesseau, L.; Jancu, J.; Bonnassieux, Y.; Katan, C.; Stoumpos, C.C.; Kanatzidis, M.G.; Even, J. Anharmonicity and disorder in the black phases of cesium lead iodide used for stable inorganic perovskite solar cells. *ACS Nano* **2018**, *12*, 3477–3486. [CrossRef] [PubMed]

44. Kulbak, M.; Cahen, D.; Hodes, G. How important is the organic part of lead halide perovskite photovoltaic cells? Efficient $CsPbBr_3$ cells. *J. Phys. Chem. Lett.* **2015**, *6*, 2452–2456. [CrossRef]

45. Jeon, N.J.; Noh, J.H.; Kim, Y.C.; Yang, W.; Ryu, S.; Seok, S.I. Solvent engineering for high-performance inorganic-organic hybrid perovskite solar cells. *Nat. Mater.* **2014**, *13*, 897. [CrossRef] [PubMed]

46. Guo, Y.; Yin, X.; Liu, J.; Wen, S.; Wu, Y.; Que, W. Inorganic CsPbIBr$_2$-based perovskite solar cells: Fabrication technique modification and efficiency improvement. *Sol. RRL* **2019**, *3*, 1900135. [CrossRef]

47. Yang, S.; Guo, Z.; Gao, L.; Yu, F.; Zhang, C.; Fan, M.; Wei, G.; Ma, T. Bifunctional dye molecule in all-inorganic CsPbIBr$_2$ perovskite solar cells with efficiency exceeding 10%. *Sol. RRL* **2019**, *3*, 1900212. [CrossRef]

48. Wang, K.; Zheng, L.; Hou, Y.; Nozariasbmarz, A.; Poudel, B.; Yoon, J.; Ye, T.; Yang, D.; Pogrebnyakov, A.V.; Gopalan, V.; et al. Overcoming Shockley-Queisser limit using halide perovskite platform? *Joule* **2022**, *6*, 756–771. [CrossRef]

49. Wang, Z.; Zhu, X.; Zuo, S.; Chen, M.; Zhang, C.; Wang, C.; Ren, X.; Yang, Z.; Liu, Z.; Xu, X.; et al. 27%-efficiency four-terminal perovskite/silicon tandem solar cells by sandwiched gold nanomesh. *Adv. Funct. Mater.* **2020**, *30*, 1908298. [CrossRef]

50. Wang, R.; Huang, T.; Xue, J.; Tong, J.; Zhu, K.; Yang, Y. Prospects for metal halide perovskite-based tandem solar cells. *Nat. Photonics* **2021**, *15*, 411–425. [CrossRef]

51. Guo, Q.; Duan, J.; Zhang, J.; Zhang, Q.; Duan, Y.; Yang, X.; He, B.; Zhao, Y.; Tang, Q. Universal dynamic liquid interface for healing perovskite solar cells. *Adv. Mater.* **2022**, *34*, 2202301. [CrossRef] [PubMed]

52. Liu, Q.; Qiu, J.; Yan, X.; Fei, Y.; Qiang, Y.; Chang, Q.; Wei, Y.; Zhang, X.; Tian, W.; Jin, S.; et al. Surface passivation and hole extraction: Bifunctional interfacial engineering toward high-performance all-inorganic CsPbIBr$_2$ perovskite solar cells with efficiency exceeding 12%. *J. Energy Chem.* **2022**, *74*, 387–393. [CrossRef]

53. Yang, C.; Wang, H.; Miao, Y.; Chen, C.; Zhai, M.; Bao, Q.; Ding, X.; Yang, X.; Cheng, M. Interfacial molecular doping and energy level alignment regulation for perovskite solar cells with efficiency exceeding 23%. *ACS Energy Lett.* **2021**, *6*, 2690–2696. [CrossRef]

54. Pan, J.; Zhang, X.; Zheng, Y.; Xiang, W. Morphology control of perovskite film for efficient CsPbIBr$_2$ based inorganic perovskite solar cells. *Sol. Energy Mater. Sol. Cells* **2021**, *221*, 110878. [CrossRef]

55. Chen, Z.; Yang, M.; Li, R.; Zang, Z.; Wang, H. Double-side interface engineering synergistically boosts the efficiency of inorganic CsPbIBr$_2$ perovskite solar cells over 12%. *Adv. Opt. Mater.* **2022**, *10*, 2200802. [CrossRef]

56. Xu, Y.; Li, G.; Jing, Y.; Zhang, H.; Wang, X.; Lu, Y.; Wu, J.; Lan, Z. n-type absorber by Cd^{2+} doping achieves high-performance carbon-based CsPbIBr$_2$ perovskite solar cells. *J. Colloid. Interface Sci.* **2022**, *608*, 40–47. [CrossRef]

57. Wang, Q.; Xu, Y.; Zhang, L.; Yang, A.; Bai, T.; Liu, F.; Lyu, M.; Zhu, J. Guanidinium thiocyanate additive engineering for high-performance CsPbIBr$_2$ solar cells with an efficiency of 10.90%. *ACS Appl. Energy Mater.* **2022**, *5*, 3110–3118. [CrossRef]

58. Liang, J.; Liu, Z.; Qiu, L.; Hawash, Z.; Meng, L.; Wu, Z.; Jiang, Y.; Ono, L.; Qi, B. Enhancing optical, electronic, crystalline, and morphological properties of cesium lead halide by Mn substitution for high-stability all-inorganic perovskite solar cells with carbon electrodes. *Adv. Energy Mater.* **2018**, *8*, 1800504. [CrossRef]

59. Guo, Y.; Zhao, F.; Wang, X.; Tao, J.; Zheng, D.; Jiang, J.; Hu, Z.; Chu, J. Multi-source cation/anion doping towards efficient carbon-based CsPbIBr$_2$ solar cells with superior open voltage up to 1.37 V. *Sol. Energy Mater. Sol. Cells* **2021**, *221*, 110918. [CrossRef]

60. Yang, X.; Xiang, H.; Huang, J.; Zhou, C.; Ran, R.; Wang, W.; Zhou, W.; Shao, Z. Thiourea with sulfur-donor as an effective additive for enhanced performance of lead-free double perovskite photovoltaic cells. *J. Colloid. Interface Sci.* **2022**, *628*, 476–485. [CrossRef]

61. Liang, J.; Zhao, P.; Wang, C.; Wang, Y.; Hu, Y.; Zhu, G.; Ma, L.; Liu, J.; Jin, Z. CsPb$_{0.9}$Sn$_{0.1}$IBr$_2$ based all-inorganic perovskite solar cells with exceptional efficiency and stability. *J. Am. Chem. Soc.* **2017**, *139*, 14009–14012. [CrossRef]

62. Liu, P.; Yang, X.; Chen, Y.; Xiang, H.; Wang, W.; Ran, R.; Zhou, W.; Shao, Z. Promoting the efficiency and stability of CsPbIBr$_2$-based all-inorganic perovskite solar cells through a functional Cu^{2+} doping strategy. *ACS Appl. Mater. Interfaces* **2020**, *12*, 23984–23994. [CrossRef]

63. Wang, D.; Li, W.; Zhang, T.; Liu, X.; Jin, X.; Xu, B.; Li, D.; Huang, Z.; Li, Q.; Lan, Z.; et al. Zinc and acetate co-doping for stable carbon-based CsPbIBr$_2$ solar cells with efficiency over 10.6%. *ACS Appl. Energy Mater.* **2022**, *5*, 2720–2726. [CrossRef]

64. Zhang, W.; Liu, H.; Qi, X.; Yu, Y.; Zhou, Y.; Xia, Y.; Cui, J.; Shi, Y.; Chen, R.; Wang, H. Oxalate pushes efficiency of CsPb$_{0.7}$Sn$_{0.3}$IBr$_2$ based all-inorganic perovskite solar cells to over 14%. *Adv. Sci.* **2022**, *9*, 2106054. [CrossRef] [PubMed]

65. Subhani, W.S.; Wang, K.; Du, M.; Liu, S. Goldschmidt-rule-deviated perovskite CsPbIBr$_2$ by barium substitution for efficient solar cells. *Nano Energy* **2019**, *61*, 165–172. [CrossRef]

66. Xiang, W.; Wang, Z.; Kubicki, D.; Tress, W.; Luo, J.; Prochowicz, D.; Akin, S.; Emsley, L.; Zhou, J.; Dietler, G.; et al. Europium-doped CsPbI$_2$Br for stable and highly efficient inorganic perovskite solar cells. *Joule* **2019**, *3*, 205–214. [CrossRef]

67. Yang, X.; Chen, Y.; Liu, P.; Xiang, H.; Wang, W.; Ran, R.; Zhou, W.; Shao, Z. Simultaneous power conversion efficiency and stability enhancement of Cs$_2$AgBiBr$_6$ lead-free inorganic perovskite solar cell through adopting a multifunctional dye interlayer. *Adv. Funct. Mater.* **2020**, *30*, 2001557. [CrossRef]

68. Jena, A.; Ishii, A.; Guo, Z.; Kamarudin, M.; Hayase, S.; Miyasaka, T. Cesium acetate-induced interfacial compositional change and graded band level in MAPbI$_3$ perovskite solar cells. *ACS Appl. Mater. Interfaces* **2020**, *12*, 33631–33637. [CrossRef]

69. Hayashi, S.; Hayamizu, K. Nuclear-magnetic-resonance chemical-shifts in alkali iodides, cuprous halides and silver-halides. *J. Phys. Chem. Solids* **1992**, *53*, 239–248. [CrossRef]

70. Tang, M.; He, B.; Dou, D.; Liu, Y.; Duan, J.; Zhao, Y.; Chen, H.; Tang, Q. Toward efficient and air-stable carbon-based all-inorganic perovskite solar cells through substituting CsPbBr$_3$ films with transition metal ions. *Chem. Eng. J.* **2019**, *375*, 121930. [CrossRef]

71. Guo, Y.; Yin, X.; Liu, J.; Que, W. Highly efficient CsPbIBr$_2$ perovskite solar cells with efficiency over 9.8% fabricated using a preheating-assisted spin-coating method. *J. Mater. Chem. A* **2019**, *7*, 19008–19016. [CrossRef]

72. Wang, R.; Zhang, H.; Han, S.; Wu, Y.; Hu, Z.; Zhang, G.; Liu, H.; He, Q.; Zhang, X. Cadmium doping for improving the efficiency and stability of carbon-based CsPbIBr$_2$ all-inorganic perovskite solar cells. *New J. Chem.* **2021**, *45*, 9243–9250. [CrossRef]

73.   Zhu, W.; Zhang, Q.; Chen, D.; Zhang, Z.; Lin, Z.; Chang, J.; Zhang, J.; Zhang, C.; Hao, Y. Intermolecular exchange boosts efficiency of air-stable, carbon-based all-inorganic planar CsPbIBr$_2$ perovskite solar cells to over 9%. *Adv. Energy Mater.* **2018**, *8*, 1802080. [CrossRef]

74.   Liu, P.; Han, N.; Wang, W.; Ran, R.; Zhou, W.; Shao, Z. High-quality Ruddlesden-Popper perovskite film formation for high-performance perovskite solar cells. *Adv. Mater.* **2021**, *33*, 2002582. [CrossRef]

75.   Gao, B.; Meng, J. Highly stable all-inorganic CsPbIBr$_2$ perovskite solar cells with 11.30% efficiency using crystal interface passivation. *ACS Appl. Energy Mater.* **2020**, *3*, 8249–8256. [CrossRef]

76.   Zhu, W.; Chai, W.; Chen, D.; Xi, H.; Chen, D.; Chang, J.; Zhang, J.; Zhang, C.; Hao, Y. Recycling of FTO/TiO$_2$ substrates: Route toward simultaneously high-performance and cost-efficient carbon-based, all-inorganic CsPbIBr$_2$ solar cells. *ACS Appl. Mater. Interfaces* **2020**, *12*, 4549–4557. [CrossRef] [PubMed]

77.   Jing, Y.; Liu, X.; Wang, D.; Li, R.; Xu, Y.; Yan, Z.; Sun, W.; Wu, J.; Lan, Z. High-efficiency and ultraviolet stable carbon-based CsPbIBr$_2$ solar cells from single crystal three-dimensional anatase titanium dioxide nanoarrays with ultraviolet light shielding function. *J. Colloid. Interface Sci.* **2022**, *616*, 201–209. [CrossRef]

78.   Zhang, C.; Wang, K.; Wang, Y.; Subhani, W.S.; Jiang, X.; Wang, S.; Bao, H.; Liu, L.; Wan, L.; Liu, S. Low-temperature crystallization of CsPbIBr$_2$ perovskite for high performance solar cells. *Sol. RRL* **2020**, *4*, 2000254. [CrossRef]

79.   Chen, Y.; Yang, X.; Liu, P.; Wang, W.; Ran, R.; Zhou, W.; Shao, Z. Improving moisture/thermal stability and efficiency of CH$_3$NH$_3$PbI$_3$-based perovskite solar cells via gentle butyl acrylate additive strategy. *Sol. RRL* **2020**, *5*, 2000621. [CrossRef]

80.   Xiang, H.; Liu, P.; Wang, W.; Ran, R.; Zhou, W.; Shao, Z. Sodium fluoride sacrificing layer concept enables high-efficiency and stable methylammonium lead iodide perovskite solar cells. *J. Mater. Sci. Technol.* **2022**, *113*, 138–146. [CrossRef]

81.   Han, Y.; Zhao, H.; Duan, C.; Yang, S.; Yang, Z.; Liu, Z.; Liu, S. Controlled n-doping in air-stable CsPbI$_2$Br perovskite solar cells with a record efficiency of 16.79%. *Adv. Funct. Mater.* **2020**, *30*, 1909972. [CrossRef]

82.   Zou, S.; Liu, Y.; Li, J.; Liu, C.; Feng, R.; Jiang, F.; Li, Y.; Song, J.; Zeng, H.; Hong, M.; et al. Stabilizing cesium lead halide perovskite lattice through Mn (II) substitution for air-stable light-emitting diodes. *J. Am. Chem. Soc.* **2017**, *139*, 11443–11450. [CrossRef] [PubMed]

83.   Guo, Y.; Wang, Q.; Saidi, W.A. Structural stabilities and electronic properties of high-angle grain boundaries in perovskite cesium lead halides. *J. Phys. Chem. C* **2017**, *121*, 1715–1722. [CrossRef]

84.   Tan, X.; Liu, X.; Liu, Z.; Sun, B.; Li, J.; Xi, S.; Shi, T.; Tang, Z.; Liao, G. Enhancing the optical, morphological and electronic properties of the solution-processed CsPbIBr$_2$ films by Li doping for efficient carbon-based perovskite solar cells. *Appl. Surf. Sci.* **2020**, *499*, 143990. [CrossRef]